Long-Term Chemothermal Stability of Delithiated NCA in Polymer Solid-State Batteries

Münir M. Besli,[a,b] Camille Usubelli,[a,c] Michael Metzger,[a] Sondra Hellstrom,[a] Sami Sainio,[d] Dennis Nordlund,[d] Jake Christensen,[a] Gerhard Schneider,[b,e] Marca M. Doeff,[f,] Saravanan Kuppan[a,*]*

[a]*Robert Bosch LLC, Research and Technology Center, Sunnyvale, California 94085, United States*
[b]*Dept. of Mech. Engineering, Karlsruhe Institute of Technology (KIT), Karlsruhe 76131, Germany*
[c]*Institute of Physics and Chemistry of Materials of Strasbourg (IPCMS), UMR 7504 CNRS, University of Strasbourg, France*
[d]*Stanford Synchrotron Radiation Lightsource, SLAC National Accelerator Laboratory, Menlo Park, California 94025, United States*
[e]*Materials Research Institute, Aalen University, Aalen 73430, Germany*
[f]*Lawrence Berkeley National Laboratory, Energy Storage and Distributed Resources Division, University of California, Berkeley, California 94720, United States*

(M.D.) E-mail mmdoeff@lbl.gov
(S.K.) E-mail saravanan.kuppan@us.bosch.com

Keywords: polymer, solid-state batteries, nickel-rich, chemothermal, NCA

In this study, the long-term chemothermal stability of chemically delithiated $Li_1Ni_{0.8}Co_{0.15}Al_{0.05}O_2$ (NCA) was systematically investigated at relevant operating temperatures of polymer solid-state batteries using *ex-situ* synchrotron-based hard and soft X-ray absorption spectroscopy. The reduction of nickel on the surface, subsurface, and in the bulk of secondary NCA particles was studied and directly related to aging time, temperature, the presence of polymeric electrolyte (poly(ethylene oxide) or polycaprolactone), and lithium salt (lithium tetrafluoroborate or lithium bis(trifluoromethanesulfonyl)imide). Depending on the polymer and/or lithium salt accompanying the delithiated $Li_{0.3}$NCA, reduction of nickel at the surface, subsurface, and bulk occurs to varying extents, starting at the surface and propagating into the bulk material. Our results indicate how degradation (reduction of nickel) is strongly correlated to temperature, time, and the presence of blended polymer and/or lithium salt in the cathode. The relative stability of the NCA material in cathodes having different polymer and lithium salt combinations identified in the *ex-situ* spectroscopy study is directly demonstrated in solid-state polymer batteries.

1. Introduction

Currently, lithium-ion batteries (LIBs) used for EVs contain a nonaqueous, liquid electrolytic solution consisting of organic solvents and lithium salts. The replacement of these liquid electrolytes with a solid-state electrolyte (SSE) is very attractive for safety and energy density reasons. The attractive properties include the possibility of using a lightweight lithium metal anode due to enhanced dendrite penetration resistance, decreased flammability,[1] and higher operating temperature range.[2] Solid polymer electrolytes (SPEs) have additional advantages in that they can be easily processed at low cost in a roll-to-roll fashion. However, they need to be operated at elevated temperatures (60 - 90 °C) to ensure sufficiently high conductivities to allow battery operation. The need for elevated temperature operation imposes material development challenges such as a need to use compatible and thermally stable electrode materials.

Although many novel cathode materials have been studied in recent years the number of suitable compounds for SPE batteries is limited.[3] Next generation solid-state batteries will most likely employ refined cathode materials that are already being used today, such as nickel-rich layered oxide materials (e.g., $LiNi_{1-x-y}Co_xAl_yO_2$ (NCA) or $LiNi_{1-x-y}Mn_xCo_yO_2$ (NMC)).[4] These materials not only offer high reversible capacities of up to 200 mAh/g, but also have high energy densities and good rate capabilities.[5] Capacities can even be extended to over 200 mAh/g when cycled to higher upper cutoff voltages such as 4.6 V vs. Li.[6] A main drawback, however, is their poor cyclability and intrinsic chemothermal instability. Ni^{4+} ions in charged nickel-rich oxides are thermodynamically unstable, particularly

during operation at elevated temperatures.[5,7,8] Thermal degradation of delithiated (charged) nickel-rich materials is additionally linked to oxygen release that is associated with several structural transformations (and reduction of nickel),[9] from a layered structure to spinel ($R\bar{3}m \rightarrow Fd\bar{3}m$) and from spinel to rock-salt ($Fd\bar{3}m \rightarrow Fm\bar{3}m$), and can become a severe safety concern.[10,11]

While the thermal stability of nickel-rich cathode materials has been investigated thoroughly using various techniques such as differential scanning calorimetry (DSC)/thermogravimetric analysis (TGA),[11–13] accelerating rate calorimetry (ARC),[14] X-ray diffraction (XRD),[12] time-resolved XRD,[13,15] and transmission electron microscopy (TEM),[16] many of these studies have focused on their high temperature stability rather than at operating temperatures relevant to SPE batteries. If these are to be used in SPE batteries, it is important to investigate their chemothermal stability at 60 – 90 ℃ and to quantify the influence of polymeric electrolyte and lithium salt on the degradation of nickel-rich cathode materials.

Previously, we have reported on the inherent thermal properties of delithiated NCA at different elevated temperatures and observed oxygen evolution and mesopore formation. We have also studied cycling induced cracking, and SOC reduction within the bulk NCA material in poly(ethylene oxide) (PEO)-based polymer solid-state batteries, due to intergranular cracking.[17,18] Herein, we report on the degradation of NCA induced by the presence of individual electrode components; i.e., polymer and lithium salt. We also studied the influence of polymer and lithium salt combinations on chemothermal NCA degradation. To carry this out, we

investigated the long-term thermal stability of delithiated $Li_{0.3}$NCA using *ex-situ* synchrotron-based hard and soft X-ray absorption spectroscopy (XAS) at the operating temperatures of polymer cells. These techniques allowed us to probe the bulk and surface oxidation states of NCA and thus to identify where improvements need to be made in order to stabilize cathode materials for use in polymer batteries. We discuss the implications of our results toward improving the cycling capabilities of polymer solid-state batteries.

2. Results

2.1. Inherent stability of $Li_{0.3}$NCA at operating conditions of polymer batteries

Hard X-ray absorption spectroscopy (hard XAS) has been widely used in materials science and also in LIB research.[19] While measuring the transition metal (TM) K-edge is especially useful for obtaining information about bulk properties, it is less sensitive to the 3d electronic states of the TMs than the $L_{2,3}$-edges, which corresponds to 2p-3d transitions;[20] more information on the 3d states can be obtained using surface dependent L-edge soft X-ray absorption spectroscopy (soft XAS). Compared to hard XAS, the penetration depth of soft XAS is very low and depends on the detection mode. For example, while the total electron yield (TEY) provides

information up to 5 nm depth, the fluorescence yield (FY) gives information further into the subsurface, since the probing depth is about 50 - 100 nm, and the primary particle sizes are around 500 nm (**Figure 1** and supplementary **Figure S1**).[21,22] A combination of the bulk (K-edge) and surface (L-edge) analysis of TMs complement each other and provide insightful, depth-dependent information on the bulk and surface structure of secondary particles in cathode materials such as NCA; due to the fairly large beam sizes (2 x 2 mm for soft XAS and 1 x 10 mm for hard XAS) and average secondary particle sizes of 6 – 10 µm, the obtained picture of the nature of the samples is more accurate than techniques that focus on just a few particles.

As seen in **Figure 2a**, nickel absorption edges in the soft XAS region result in two distinct peaks, L_3 and L_2, which correspond to transitions from $2p_{2/3}$ and $2p_{1/2}$ into 3d orbitals, respectively. The nature of this splitting is due to the spin-orbit interaction of the core hole.[23] Additional splitting into a multiplet structure of the L_3- and L_2-edges is due to crystal field effects and 2p-3d interactions.[24] The intensity ratio of the two peaks in the L_3-edge, $L_{3,\,high}/L_{3,\,low}$, is proportional to the valence state of the absorbing species. To retrieve valence state information of the top surface and subsurface, $L_{3,\,high}/L_{3,\,low}$ peak ratios can be calculated and linked to reference standards with known oxidation states.[25] Examples are shown in Figure 2a for nickel oxide (NiO), pristine NCA, and chemically delithiated NCA, in which the nickel oxidation states are 2+, 3+, and 3.7+, respectively. By relating $L_{3,\,high}/L_{3,\,low}$ peak ratios to reference substances with known nickel oxidation

states, the ratios can be used to estimate the oxidation state of aged NCA samples (see supplementary **Figure S2a-b**). A decrease in the peak ratio compared to the initial valence state indicates reduction of nickel due to decomposition. Depending on the detection mode, the observed decomposition can vary (see Figure 1b). Sicklinger et al. showed how the top layer of the secondary particles usually consists of surface contaminations such as hydrated nickel carbonate-hydroxides or Li_2CO_3 due to air exposure (which cannot be fully prevented due to the synthesis and storage conditions used for the commercial sample).[26] Usually such surface contaminants result in a more reduced top surface layer. This can be probed by auger electron yield (AEY, 2 nm), but this was not used in this study because the oxidation state is strongly affected by surface contaminants. In addition, the well-described phenomenon of surface reconstruction, which describes the tendency for nickel-rich oxide particles to transition from their initial layered phase to a rock salt phase on the surface, also affects results using AEY and TEY modes.[27] In this study, we focused on the TEY and FY mode derived data for more accurate pictures of the extent of reduction happening in the surface and at the subsurface of secondary NCA particles, respectively.

In contrast to this, the nickel absorption edge in the hard XAS region is a result of the excitation of the metal 1s electron into the continuum state or into a valence orbital.[28] In addition to the strong, dipole-allowed absorption edge containing information on the valence state of the absorbing metal, the absorption spectrum also contains a dipole-forbidden transition of a

metal 1s electron into a 3d orbital, which results in a small pre-edge feature.[29–31] The rising-edge is of particular interest, since it can be linked to the oxidation state of the absorbing TM; changes in the rising-edge absorption help to better understand valence state changes in the bulk material during aging.[17,18,32–34] As seen in Figure 2b, a higher nickel oxidation state leads to a higher K-edge absorption energy than a lower nickel oxidation state (also see supplementary Figure S2c). In addition, the determined nickel oxidation state can then be used as a proxy for apparent oxidation state estimations as charge compensation comes primarily from the nickel in NCA, as reported in the literature.[35–37] For this purpose, either the K-edge energy values for the top of the peak, the half-height of the rising edge at a normalized absorption value of 0.5, or, as applied in this study, the K-edge energy values for the inflection point of the first derivative can be used and linked to the oxidation state.[35,38]

Pristine NCA ($Li_1Ni_{0.8}Co_{0.15}Al_{0.05}O_2$) cathode material of commercial quality was 70% delithiated (unless otherwise noted, 'delithiated NCA' refers to chemically delithiated NCA with a composition of $Li_{0.3}$NCA) and the chemical composition subsequently determined to $Li_{0.29}Ni_{0.79}Co_{0.15}Al_{0.04}O_2$ ($Li_{0.3}$NCA) using inductively coupled plasma-optical emission spectroscopy (ICP-OES). $Li_{0.3}$NCA powder was then aged by storing it at various temperatures and for different times and analyzed using soft nickel L-edge XAS and hard nickel K-edge XAS. **Figure 3a and 3b** show the changes happening for $Li_{0.3}$NCA at the surface (TEY, 5 nm) shown in red and subsurface (FY, 50 – 100 nm) shown in blue, respectively, using L_3-edge

peak ratios for samples stored between 2 and 49 days at various temperatures. For quantification purposes, TEY and FY L_3-edge ratios of pristine nickelate standards (shown in supplementary Figure S2a-b) and $Li_{0.3}$NCA were linked to the calculated oxidation states and linearly interpolated (see Figure 3c-d). Using this linear interpolation, L_3-edge ratios for aged samples were used to determine the apparent oxidation state. Additionally, $Li_{0.3}$NCA (30% lithiated, nickel = 3.7+) and pristine Li_1NCA (100% lithiated, nickel = 3+) were used analogously for a fully charged polymer battery (4.2 V) and a fully discharged polymer battery (3.0 V) to correlate the L_3-edge ratios to degree of aging (see Figure 3e-f). Resulting apparent oxidation states (and degree of aging) for aged samples shown in Figure 3e-f indicate that $Li_{0.3}$NCA exhibits a strongly temperature- and time-dependent reduction of nickel, both at the surface (TEY, 5 nm) and the subsurface (FY, 50 – 100 nm), while reduction at the surface (TEY) is slightly higher than in the subsurface (FY).

In addition to the degradation observed within the first 50 days, $Li_{0.3}$NCA samples were additionally analyzed after aging for a total time of four months and also one year. Since most of the commercially available dry polymer electrolyte LIBs (typically using lithium iron phosphate cathodes) operate at 80 °C,[39–41] long-term aging was only carried out at 80 °C. **Figure 4** shows the apparent oxidation states and the correlated degrees of aging for $Li_{0.3}$NCA samples stored for up to 1 year at 80 °C. Similar to Figure 3, FY derived apparent oxidation states (blue data in Figure 4) show that there was less reduction upon storage at the subsurface than at the

surface (TEY derived peak ratios (red)). This implies that the top surface of the cathode particles (probed by TEY) is always more reduced than the subsurface (probed by FY), which is due to the previously mentioned surface reconstruction.[27] TEY derived peak ratios of long-term aged samples are very similar to the ratios for samples stored for a total time of 49 days, indicating that not much reduction of nickel occurs beyond 49 days of aging (compare also data in Figure 3e and 3f). The average apparent nickel oxidation state for the surface and subsurface after 1 year is approximately +3.23 (approx. 67% degree of aging).

Figure 5 shows the normalized nickel K-edge X-ray absorption near edge structure (XANES) spectra for $Li_{0.3}$NCA and pristine NCA stored at 80 °C for up to 1 year along with freshly prepared $Li_{0.3}$NCA shown as a reference (see also supplementary **Figure S3** for XANES spectra of samples aged at 60 and 90 °C). As indicated above, a shift of the nickel K-edge towards lower energies, as shown in Figure 5a, indicates a reduction of the X-ray absorbing nickel atoms in the bulk material. Within the first 49 days, little reduction occurs in the bulk but this is followed by significant shifts after 4 months and 1 year. Using the linear relationship between the nickel K-edge energy and the oxidation state (see supplementary Figure S2c for hard XAS spectra of common nickel-rich layered oxide standards), we have quantified the amount of reduction happening in Figure 5b using pristine Li_1NCA (nickel = 3+) and $Li_{0.3}$NCA (nickel = 3.7+). Determined nickel oxidation state values show no clear trend for the first 49 days and are independent of storage temperatures. Thus, the clear trend originally

observed with the surface sensitive techniques (Figure 3 and 4) is not reflected in the bulk. This result also shows that the bulk effects clearly dominate over surface effects in a technique like hard XAS that probes the entire particle, due to the much larger volume fraction of bulk to surface and subsurface (see Figure 1a). Only samples subjected to 4 months of aging at 80 °C show a clear reduction in the measured nickel oxidation state, which does not substantially change further when samples are kept at 80 °C for 1 year. This observation is in good agreement with our previous study, where we demonstrated the short-term thermal stability of $Li_{0.3}$NCA at 200 °C.[17]

2.2. Stability of $Li_{0.3}NCA$ in presence of PEO and lithium salt ($LiBF_4$, LiTFSI)

To investigate the influences of polymer and lithium salt, which are components of composite cathodes for polymer batteries, we have studied $Li_{0.3}NCA$ with polymer and lithium salt separately and combined. For this purpose, several cathode mixtures consisting of $Li_{0.3}NCA$ blended with polymer, $Li_{0.3}NCA$ blended with polymer (PEO) plus lithium salt (either lithium tetrafluoroborate ($LiBF_4$), or lithium bis(trifluoromethanesulfonyl)imide (LiTFSI)), or with these salts alone, were prepared and subsequently stored at 80 °C for 35 days. Weight ratios of each composition tested were based on mixtures typically used in polymer lithium-metal batteries and can be found in the experimental section. Oxidation state changes at the surface, subsurface, and in the bulk of delithiated NCA particles were quantified using soft XAS and hard XAS. It is important to note here, that the chosen storage conditions for NCA are very harsh; for example, over a period of 2 years for a polymer battery which is charged once a day and spends approx. 1 hour at a highly charged (delithiated) state, the total time spent at this state would sum up to about 30 days. Within this time span, very little degradation would occur in the bulk of the NCA material, although the surface would show extensive reduction (this is only an example, and the amount of time spent at a high delithiation state is strongly dependent on the application).

Figure 6a shows the amount of reduction happening at the surface (TEY, red) and subsurface (FY, blue) for $Li_{0.3}NCA$ powder in combination with

PEO. In the presence of PEO alone, the surface and subsurface indicate an apparent nickel oxidation state of +2.41 and +2.70, respectively, below the valence of pristine NCA (+3). In comparison, for $Li_{0.3}$NCA in the absence of polymer, after 35 days of storage, the apparent nickel oxidation state at the surface and subsurface were +3.38 and +3.39 (see Figure 3e-f, complete set of valence states can be found in supplementary **Table S1**).

In the presence of $LiBF_4$ alone (see Figure 6b), the reduction is less severe than in presence of PEO alone (Figure 6a) or for $Li_{0.3}$NCA without any polymer or lithium salt (Figure 3e-f). This indicates that $Li_{0.3}$NCA is stabilized by the presence of $LiBF_4$. In contrast to this, with LiTFSI (Figure 6b), the reduction of nickel at the surface to +2.54 and at the subsurface to +3.03 is more severe.

When PEO is combined with $LiBF_4$ or LiTFSI (Figure 6c) and mixed with $Li_{0.3}$NCA, the cathode material appears to age faster than when it is alone or mixed with $LiBF_4$. The surface and subsurface stabilities after 35 days at 80 °C can be arranged in the order:

$Li_{0.3}$NCA-$LiBF_4$ > $Li_{0.3}$NCA > $Li_{0.3}$NCA-PEO-$LiBF_4$ > $Li_{0.3}$NCA-PEO-LiTFSI > $Li_{0.3}$NCA-LiTFSI > $Li_{0.3}$NCA-PEO

When PEO is present in the mixture, the $Li_{0.3}$NCA bulk degraded the most (see **Figure 7**, also see supplementary **Figure S4** for hard XAS spectra). When PEO and lithium salts were used in the mixture, the degree of aging

was not as great as with PEO only, whereas PEO-LiTFSI (yellow), showed higher degrees of aging than PEO-$LiBF_4$. This follows the degradation trend observed for the surface and subsurface using soft XAS. In keeping with that trend, the bulk, similar to the surface and subsurface regions, showed excellent stability and minimal reduction for delithiated NCA mixed with $LiBF_4$ alone (green). Surprisingly, the bulk materials also show little degradation with LiTFSI (red), while the surface and subsurface showed a very drastic reduction happening within 35 days.

In summary, the bulk stabilities after 35 days at 80 °C can be arranged in the order:

$Li_{0.3}$NCA-$LiBF_4$ ≈ $Li_{0.3}$NCA > $Li_{0.3}$NCA-LiTFSI > $Li_{0.3}$NCA-PEO-$LiBF_4$ > $Li_{0.3}$NCA-PEO-LiTFSI > $Li_{0.3}$NCA-PEO

2.3. Stability of $Li_{0.3}$NCA in the presence of PCL and lithium salt

To see if $Li_{0.3}$NCA in combination with other polymers show the same degree of degradation (with and without lithium salts), we have conducted several studies with numerous polymers and lithium salts, and present here one example using polycaprolactone (PCL) in **Figure 8**. When comparing the results for PCL (Figure 8a) and PEO (Figure 6a), the degradation seems to be less severe for PCL. The surface and subsurface regions for the $Li_{0.3}$NCA particles show a reduction of the initial oxidation state to +3.18 and +3.29, respectively, much less than that with PEO (+2.41 and +2.70 at the surface and subsurface, respectively). $Li_{0.3}$NCA also shows improved stability with PCL-$LiBF_4$ compared to PEO-$LiBF_4$

(Figure 8b). As an example, after 35 days of aging, $Li_{0.3}NCA$ in a matrix of PCL and $LiBF_4$, only showed a reduction of the initial oxidation state to +3.46 and +3.52 for the surface and subsurface, respectively. PEO-$LiBF_4$, in contrast, showed a reduction of the surface and subsurface nickel oxidation state to +3.24 and +3.29, respectively. This indicates that PCL in combination with $LiBF_4$ is almost two times more stable than PEO-$LiBF_4$ in contact with the highly oxidizing $Li_{0.3}NCA$. In summary, the surface and subsurface stabilities of $Li_{0.3}NCA$ in the presence of PEO, PCL, and lithium salt can be arranged in the order:

$Li_{0.3}NCA$-$LiBF_4$ ≈ $Li_{0.3}NCA$-PCL-$LiBF_4$ > $Li_{0.3}NCA$ > $Li_{0.3}NCA$-PEO-$LiBF_4$ > $Li_{0.3}NCA$-PCL > $Li_{0.3}NCA$-PEO-LiTFSI > $Li_{0.3}NCA$-LiTFSI > $Li_{0.3}NCA$-PEO

The observed stability increase with PCL could also be seen when analyzing the degradation in the bulk. Figure 8c shows that the average nickel oxidation state in the bulk state is reduced to +3.57 for PCL-$LiBF_4$ after 35 days, while PEO-LiTFSI dropped to +3.21, respectively. This suggests a three times higher stability of PCL over PEO also in terms of the bulk oxidation state retention. The enhanced stability of PCL was also reflected in the electrochemical cycling of NCA/PCL-$LiBF_4$//Li cells. Figure 8d compares the capacity retention of NCA/PCL-$LiBF_4$//Li cells compared to NCA/PEO-LiTFSI//Li cells cycled at a rate of C/6 and 80 °C. While the PEO cell shows significantly reduced capacity within the first 20 cycles, the PCL cell could be cycled well over 80 times with >80% capacity retention.[18]

2.4. Stability of NMC622 and NMC811 in the presence of PCL and lithium salt

To see if the enhanced chemothermal stability of $Li_{0.3}$NCA in contact with PCL and $LiBF_4$ is also transferable to other commercially relevant nickel-rich layered oxide materials, we have also combined delithiated $Li_{0.3}Ni_{0.8}Mn_{0.1}Co_{0.1}O_2$ ($Li_{0.3}$NMC811) and $Li_{0.3}Ni_{0.6}Mn_{0.2}Co_{0.2}O_2$ ($Li_{0.3}$NMC622) with PCL and/or $LiBF_4$, respectively. An overview of the surface and bulk oxidation state retention of nickel in $Li_{0.3}$NMC811 and $Li_{0.3}$NMC622 is given in **Figure 9** and below.

The surface stabilities of $Li_{0.3}$NMC811 and $Li_{0.3}$NMC622 in the presence of PCL and/or lithium salt can be arranged in the order (Figure 9a and d):

$Li_{0.3}$NMC622-$LiBF_4$ > $Li_{0.3}$NMC622-PCL-$LiBF_4$ > $Li_{0.3}$NMC622-PCL > $Li_{0.3}$NMC811-PCL-$LiBF_4$ > $Li_{0.3}$NMC811-$LiBF_4$ > $Li_{0.3}$NMC811-PCL

The subsurface stabilities of $Li_{0.3}$NMC811 and $Li_{0.3}$NMC622 in the presence of PCL and/or lithium salt can be arranged in the order (Figure 9b and e):

$Li_{0.3}$NMC622-$LiBF_4$ > $Li_{0.3}$NMC811-$LiBF_4$ > $Li_{0.3}$NMC811-PCL-LiBF4 ≈ Li0.3NMC622-PCL-$LiBF_4$ > $Li_{0.3}$NMC622-PCL > $Li_{0.3}$NMC811-PCL

Bulk stabilities of $Li_{0.3}$NMC811 and $Li_{0.3}$NMC622 in the presence of PCL and/ or lithium salt can be arranged in the order (Figure 9c and f):

$Li_{0.3}$NMC811-PCL-$LiBF_4$ ≈ $Li_{0.3}$NMC622-$LiBF_4$ ≈ $Li_{0.3}$NMC811-$LiBF_4$ ≈ Li-$_{0.3}$NMC622-PCL-$LiBF_4$ > $Li_{0.3}$NMC622-PCL > $Li_{0.3}$NMC811-PCL

Similar to the observed stability enhancement for $Li_{0.3}$NCA blended with PCL and $LiBF_4$ (Figure 8), NMC622 and NMC811 also showed increased surface, subsurface and bulk stabilities. Our results indicate the importance of the use of a chemothermally stable polymer along with the appropriate lithium salt ($LiBF_4$) for solid-state polymer batteries and are summarized for $Li_{0.3}$NCA in **Figure 10** (also see supplementary **Table S2**).

3. Discussion

3.1. Surface and bulk degradations for $Li_{0.3}$NCA without polymer or lithium salt

The less stable surface of the $Li_{0.3}$NCA particles, as observed in Figure 3 and 4, can most likely be explained by a core-shell model, in which the degradation of layered oxide materials is initiated by a transition from layered phase to a spinel or rock salt phase from surface to bulk, also called surface reconstruction.[27,42] This phase transformation is due to rearrangement of TM atoms but also triggered by lattice oxygen release, as previously reported in the literature.[5,22,27,43,44] Cathode materials that are at a high delithiation state are especially prone to this phase transition.[44,45] The chemically delithiated $Li_{0.3}$NCA at elevated temperatures undergoes structural transformations involving oxygen evolution and reduction of nickel. Our results indicate that the phase transformation, and the associated nickel reduction, starts at the surface and propagates into the bulk material with increased aging time, in accordance with the literature.[44] Our previous study showed the onset of oxygen evolution from $Li_{0.3}$NCA occurs at 200 °C using TGA-MS.[17] Although in this study samples are stored at 60 - 90 °C, it cannot be ruled out that a small amount of oxygen escapes from the surface at these temperatures and long storage times, initiating decomposition at the surface. The release of oxygen from the crystal lattice may be exacerbated at a low partial oxygen pressure, i.e., the storage in an inert atmosphere as was done in this study. However, more definitive experiments, such as a long-term TGA-MS study, would be required to validate this.

3.2. Surface and bulk degradations for $Li_{0.3}$NCA blended with PEO

The surface and bulk regions of $Li_{0.3}$NCA exhibit the poorest chemothermal stabilities when PEO is present. The most plausible explanation for this is the well-established poor oxidative stability of PEO above 4 V, as discussed in the literature on polymer cells.[46] As mentioned in the results section, $Li_{0.3}$NCA is equal to electrochemically delithiated NCA at a potential of 4.2 V vs. Li^+/Li. At this highly delithiated state, PEO in contact with highly oxidizing $Li_{0.3}$NCA is irreversibly oxidized, reducing nickel in $Li_{0.3}$NCA. With continuous PEO oxidation, more and more $Li_{0.3}$NCA surface domains are reduced, which eventually leads to a phase transformation and release of oxygen as seen in **Equation 1**.

$$Li_{0.3}Ni^{3.7+}O_2 \rightarrow Li_{0.3}Ni^{(3.7-y)+}O_{(2-y)} + y/2\ O_2\uparrow \quad (1)$$

Equation 1 cannot explain the observed bulk reduction of nickel in the presence of PEO. Although above its melting point (65 °C) PEO behaves like a gel-like substance, to what extent it can infiltrate the active material secondary particle and lead to bulk reduction is unknown.

3.3. Surface and bulk degradations for $Li_{0.3}$NCA blended with lithium salts

An interesting finding is the fact that when $Li_{0.3}$NCA was only mixed with $LiBF_4$ or LiTFSI salts without polymer; less nickel reduction was obtained with $Li_{0.3}$NCA-$LiBF_4$ compared to $Li_{0.3}$NCA-LiTFSI. Furthermore, using only $LiBF_4$ as an additive showed the least degradation in surface, subsurface,

and bulk. The use of $LiBF_4$ results in good cyclability of liquid electrolyte containing lithium-ion batteries, but is also known to reduce parasitic reactions and increase performance of batteries at high operating voltages and a wide temperature range.[47–53] In the case described in this paper, where the cathode does not undergo electrochemical cycling, $LiBF_4$ could still slow nickel reduction due to passivation effects.

LiTFSI, in contrast, has a lower thermal stability with an onset initial temperature at which free acid bound to the salt is released at 36 °C, as shown by Lu et al.[54] The higher amount of free acid bound to LiTFSI released at lower temperatures in the form of HF could explain the severe surface degradation observed, since HF within fluorine containing electrolyte is known to attack cathode particles forming lithium or transition metal fluorides.[55–58] More extensive studies are needed in order to gain further insight into the role of lithium salts and polymer on the degradation of cathode active material employed in polymer batteries at relevant operating temperatures.

3.4. Surface and bulk degradations for $Li_{0.3}$NCA blended with PEO and lithium salt

The combination of both, polymer and salt, shows to compensate each other. While PEO shows to degrade and reduce nickel as described above, the salts seem to compensate the effect. This is especially true for $LiBF_4$, whereas LiTFSI shows to have a little stabilizing effect on the harsh degradation in presence of PEO.

3.5. Surface and bulk degradations for $Li_{0.3}$NCA blended with PCL and lithium salt

The reduction of nickel in $Li_{0.3}$NCA was less severe when blended with PCL, compared to PEO. This is due to the higher oxidative stability of PCL; for example, a polymer solid-state cell containing PCL could be charged to 4.5 V and showed a long time stability.[59] $Li_{0.3}$NCA with PEO alone showed the most extensive nickel reduction at the surface and subsurface, and in the bulk, while blending PCL and $LiBF_4$ with $Li_{0.3}$NCA showed the best Ni oxidation state retention of all the combinations studied. This improved stability is reflected in the better cycling seen for cells with PCL-$LiBF_4$ compared to PEO-LiTFSI in Figure 8d.

3.6. Surface and bulk degradations for NMC622 and NMC811 blended with PCL and lithium salt

Other delithiated nickel-rich cathode materials such as $Li_{0.3}$NMC622 and $Li_{0.3}$NMC811 also showed similar stability results like those obtained for $Li_{0.3}$NCA. In both cases, $Li_{0.3}$NMC622 and $Li_{0.3}$NMC811 combined with PCL and $LiBF_4$ showed similar nickel reduction trends as for $Li_{0.3}$NCA with PCL and $LiBF_4$. The high stability for $Li_{0.3}$NMC622 in the presence of PCL only is consistent with the fact that with increasing nickel content, cathode materials are thermally less stable.[60]

4. Conclusion

Hard and soft X-ray absorption spectroscopy were used to probe the nickel valence state changes of chemically delithiated NCA aged alone, and in a variety of combinations with polymer and lithium salt. By analyzing the valence state changes for nickel located at the surface and subsurface, and in the bulk regions, we showed how the chemothermal degradation of the active material begins at the surface and seems to propagate into the bulk material. Depending on the additional components (polymer and/or lithium salt) blended with the delithiated cathode active material, the surface reconstruction at 80 °C can be hindered to a certain degree. Blending in polymers accelerated nickel reduction at the surface and subsurface, and in the bulk, particularly in the case of PEO. In contrast, blending in only lithium salts with the delithiated cathode materials resulted in less nickel reduction in the case of $LiBF_4$, and more distinct reduction for LiTFSI. In terms of the ‘use case’, i.e., a solid-state polymer battery with cathode active material, polymer and lithium salt, we identified PCL-$LiBF_4$ as a promising catholyte for NCA//Li polymer cells and showed the importance of the chemothermal interplay of all three components within the cell. Although further experiments are needed to shed light on the underlying degradation phenomena and the interplay of all components, our methodology of a quick screening of the nickel reduction within the cathode active material using soft and hard XAS can directly be applied into solid-state polymer battery development.

5. Experimental Section

Chemical delithiation:

A commercial sample of pristine NCA cathode active material was chemically delithiated to $Li_{0.3}NCA$ by oxidation with a 0.1 M solution of nitronium tetrafluoroborate (NO_2BF_4; Sigma-Aldrich, USA) in acetonitrile (ACN; Sigma-Aldrich, USA) for 24 hours in an Argon filled glove box (O_2 < 0.1 ppm, H_2O < 0.1 ppm) at room temperature. The lithium ratio in NCA is governed by the ratio of NCA to NO_2BF_4 during the oxidation reaction:

$$Li_1Ni^{3+}O_2\ (30\%) + NO_2BF_4(70\%) \rightarrow Li_{0.3}Ni^{3.7+}O_2 + Li_{0.7}BF_4 + NO_2\uparrow \quad (2)$$

Delithiated NCA powders were separated from the solution by filtering and centrifugation and thoroughly washed afterwards with ACN. The washed powder was subsequently dried overnight in a vacuum oven at room temperature. The chemical composition of the pristine and delithiated NCA samples (residual Li and transition metal ratio) was subsequently determined using inductively coupled plasma-optical emission spectroscopy (Thermo Scientific™ iCAP™ 7000 ICP-OES). Elemental composition of pristine NCA and delithiated NCA was determined to be $Li_{1.03}Ni_{0.79}Co_{0.15}Al_{0.04}$ and $Li_{0.29}Ni_{0.79}Co_{0.15}Al_{0.04}$ (referred to as $Li_{0.3}NCA$ in here), respectively. Phase purity and morphology were analyzed using X-ray diffraction (XRD, Bruker D8 ADVANCE) and scanning electron microscopy (SEM, JEOL USA JSM-7200F).

Sample preparation:

In an argon filled glovebox (O_2 < 0.1 ppm, H_2O < 0.1 ppm) delithiated NCA ($Li_{0.3}$NCA) was weighed into airtight coin cells, crimped, and subsequently double sealed in thermally stable pouches. Several batches for the individual sampling times were prepared. Similar to this, $Li_{0.3}$NCA-lithium salt compositions were prepared by first dissolving the respective lithium salt in ACN, and then adding delithiated NCA to the solution. The mixture was then vacuum dried in the glovebox antechamber, without exposing the material to air, and then weighed into airtight coin cells, crimped, and double sealed similar as described above. For $Li_{0.3}$NCA-polymer and $Li_{0.3}$NCA-polymer-lithium salt mixtures, first the lithium salt and/or polymer was dissolved in ACN. The weight ratios of $Li_{0.3}$NCA:polymer:lithium salt was chosen to be exactly the same as used for the preparation of polymer cells; $Li_{0.3}$NCA:PEO:$LiBF_4$, 77:20:3, wt%; $Li_{0.3}$NCA:PEO:LiTFSI, 77:16:7, wt%; $Li_{0.3}$NCA:PCL:LiTFSI, 77:16:7, wt%. After full dissolution of the polymer and/ or lithium salt, delithiated NCA was added to the solution and in a final step, the solution was coated on aluminum foil. The coated sheet was then vacuum dried in the glovebox antechamber without exposure to air. A small disc was then punched and, similar as described above, crimped in an airtight coin cell and double sealed in a thermally stable pouch bag. Sealed samples were then transferred into temperature chambers outside of the glovebox and stored at 60, 80, or 90 °C and subsequently analyzed after certain storage times using soft L-edge XAS and hard K-edge XAS.

Synchrotron characterization

Soft X-ray absorption spectroscopy:

For soft XAS measurements, a thin layer of pristine NCA, as-prepared delithiated $Li_{0.3}$NCA as well as all aged samples and standards (if powder), or a piece of 5 x 5 mm sample (if coated on aluminum foil) was spread or stuck onto a conductive carbon tape which was then attached to an aluminum sample holder inside an argon filled glovebox (O_2 < 0.1 ppm, H_2O < 0.1 ppm). Measurements for nickel L-edge were carried out at the 31-pole wiggler beamline 10-1 at the Stanford Synchrotron Radiation Lightsource (SSRL) with a spherical grating monochromator with 20 mm entrance and exit slits, a 0.2 eV energy resolution and a 2 x 2 mm beam spot. Data were collected at room temperature under ultrahigh vacuum (10^{-9} Torr) in a single load using the total electron yield (TEY) and fluorescence yield (FY) mode detectors.

Hard X-ray absorption spectroscopy:

Hard XAS data on nickel K-edge was collected in transmission mode using a Si (220) monochromator at SSRL beamline 2-2 and 4-1. Pristine NCA, as-prepared delithiated $Li_{0.3}$NCA as well as all samples and standards in powder form were carefully dispersed on Kapton films; samples coated on aluminum foil were carefully transferred on Kapton films. All sample handling was conducted in an argon filled glovebox (O_2 < 0.1 ppm, H_2O < 0.1 ppm). Higher harmonics in the X-ray beam were rejected by detuning the Si (220) monochromator by 40% at the nickel K-edge. Energy

calibration was accomplished by using the first inflection points in the spectra of nickel metal foil reference at 8332.8 eV. XANES data were analyzed by Sam's Interface for XAS Package (SIXPACK),[61] with the photoelectron energy origin (E_0) determined by the first inflection point of the absorption edge jump. Prior to data acquisition, samples were mounted into a sample box with flowing inert gas.

Preparation of polymer cells:

NCA-PEO//Li and NCA-PCL//Li pouch cells were prepared as described in previous literature,[7,18,62,63] a polystyrene (PS)−PEO separator was used in combination with PEO or PCL binder (electrolyte), respectively.

Electrochemical cycling:

The pouch cells were cycled with an Arbin BT2043 tester at 80 °C. Galvanostatic cycling was performed at a rate of C/6 referring to a practical capacity of NCA of 180 mAh/g between 3 and 4.2 V; this C-rate corresponds to a current density of 100 μA/cm^2. A stack pressure of 5 psi was applied during electrochemical cycling. No difference in electrochemical performance was found at higher stack pressures.

Acknowledgements

The synchrotron experiments of this research were performed at the Stanford Synchrotron Radiation Lightsource (SSRL), a Directorate of SLAC National Accelerator Laboratory and an Office of Science User Facility operated for the U.S. Department of Energy Office of Science by Stanford

University. Use of the Stanford Synchrotron Radiation Lightsource, SLAC National Accelerator Laboratory, is supported by the U.S. Department of Energy, Office of Science, Office of Basic Energy Sciences under Contract DE-AC02-76SF00515. Work at the Molecular Foundry was supported by the Office of Science, Office of Basic Energy Sciences, of the U.S. Department of Energy under Contract DE-AC02-05CH11231.

References

1 T. Inoue and K. Mukai, *ACS Appl. Mater. Interfaces*, 2017, **9**, 1507–1515.

2 V. Thangadurai and W. Weppner, *Ionics (Kiel).*, 2006, **12**, 81–92.

3 B. Xu, D. Qian, Z. Wang and Y. S. Meng, *Mater. Sci. Eng. R Reports*, 2012, **73**, 51–65.

4 D. Andre, S.-J. Kim, P. Lamp, S. F. Lux, F. Maglia, O. Paschos and B. Stiaszny, *J. Mater. Chem. A*, 2015, **3**, 6709–6732.

5 A. Manthiram, B. Song and W. Li, *Energy Storage Mater.*, 2017, **6**, 125–139.

6 M. M. Thackeray, S.-H. Kang, C. S. Johnson, J. T. Vaughey, R. Benedek and S. A. Hackney, *J. Mater. Chem.*, 2007, **17**, 3112–3125.

7 S.-L. Wu, A. E. Javier, D. Devaux, N. P. Balsara and V. Srinivasan, *J. Electrochem. Soc.*, 2014, **161**, A1836–A1843.

8 J. W. Fergus, *J. Power Sources*, 2010, **195**, 4554–4569.

9 R. Jung, M. Metzger, F. Maglia, C. Stinner and H. A. Gasteiger, *J. Electrochem. Soc.*, 2017, **164**, A1361–A1377.

10 I. Belharouak, D. Vissers and K. Amine, *J. Electrochem. Soc.*, 2006, **153**, A2030.

11 I. Belharouak, W. Lu, D. Vissers and K. Amine, *Electrochem. commun.*, 2006, **8**, 329–335.

12 Z. Li, N. A. Chernova, J. Feng, S. Upreti, F. Omenya and M. S. Whittingham, *J. Electrochem. Soc.*, 2012, **159**, A116–A120.

13 S. Myung, K. Lee, C. S. Yoon, Y. Sun, K. Amine and H. Yashiro, *J. Phys. Chem. C*, 2010, **114**, 4710–4718.

14 Y. Wang, J. Jiang and J. R. Dahn, *Electrochem. commun.*, 2007, **9**, 2534–2540.

15 S. M. Bak, K. W. Nam, W. Chang, X. Yu, E. Hu, S. Hwang, E. A. Stach, K. B. Kim, K. Y. Chung and X. Q. Yang, *Chem. Mater.*, 2013, **25**, 337–351.

16 J. D. Steiner, L. Mu, J. Walsh, M. M. Rahman, B. Zydlewski, F. M. Michel, H. L. Xin, D. Nordlund and F. Lin, *ACS Appl. Mater. Interfaces*, 2018, **10**, 23842–23850.

17 M. M. Besli, A. K. Shukla, C. Wei, M. Metzger, J. Alvarado, J. Boell, D. Nordlund, G. Schneider, S. Hellstrom, C. Johnston, J. Christensen, M. M. Doeff, Y. Liu and S. Kuppan, *J. Mater. Chem. A*, 2019, **7**, 12593–12603.

18 M. M. Besli, S. Xia, S. Kuppan, Y. Huang, M. Metzger, A. K. Shukla, G. Schneider, S. Hellstrom, J. Christensen, M. M. Doeff and Y. Liu, *Chem. Mater.*, 2019, **31**, 491–501.

19 F. Lin, Y. Liu, X. Yu, L. Cheng, A. Singer, O. G. Shpyrko, H. L. Xin, N. Tamura, C. Tian, T. C. Weng, X. Q. Yang, Y. S. Meng, D. Nordlund, W. Yang and M. M. Doeff, *Chem. Rev.*, 2017, **117**, 13123–13186.

20 D. Asakura, E. Hosono, Y. Nanba, H. Zhou, J. Okabayashi, C. Ban, P. A. Glans, J. Guo, T. Mizokawa, G. Chen, A. J. Achkar, D. G. Hawthron, T. Z. Regier and H. Wadati, *AIP Adv.*, , DOI:10.1063/1.4943673.

21 C. Wei, Y. Zhang, S.-J. Lee, L. Mu, J. Liu, C. Wang, Y. Yang, M. Doeff, P. Pianetta, D. Nordlund, X. Du, Y.-C. Tian, K. Zhao, J.-S. Lee, F. Lin and Y. Liu, *J. Mater. Chem. A*, 2018, **6**, 23055–23061.

22 F. Lin, D. Nordlund, I. M. Markus, T. C. Weng, H. L. Xin and M. M.

Doeff, *Energy Environ. Sci.*, 2014, **7**, 3077–3085.

23 W.-S. Yoon, O. Haas, S. Muhammad, H. Kim, W. Lee, D. Kim, D. A. Fischer, C. Jaye, X.-Q. Yang, M. Balasubramanian and K.-W. Nam, *Sci. Rep.*, 2015, **4**, 6827.

24 J. Van Elp, B. G. Searle and Z. H. Zbou, *J. Am. Chem. Soc.*, 1994, **116**, 1918–1923.

25 S. Kuppan, H. Duncan and G. Chen, *Phys. Chem. Chem. Phys.*, 2015, **17**, 26471–26481.

26 J. Sicklinger, M. Metzger, H. Beyer, D. Pritzl and H. A. Gasteiger, *J. Electrochem. Soc.*, 2019, **166**, A2322–A2335.

27 F. Lin, I. M. Markus, D. Nordlund, T.-C. Weng, M. D. Asta, H. L. Xin and M. M. Doeff, *Nat. Commun.*, 2014, **5**, 3529.

28 M. L. Baker, M. W. Mara, J. J. Yan, K. O. Hodgson, B. Hedman and E. I. Solomon, *Coord. Chem. Rev.*, 2017, **345**, 182–208.

29 K.-W. Nam, S.-M. Bak, E. Hu, X. Yu, Y. Zhou, X. Wang, L. Wu, Y. Zhu, K.-Y. Chung and X.-Q. Yang, *Adv. Funct. Mater.*, 2013, **23**, 1047–1063.

30 M. G. Kim and C. H. Yo, *J. Phys. Chem. B*, 1999, **103**, 6457–6465.

31 K. Saravanan, A. Jarry, R. Kostecki and G. Chen, *Sci. Rep.*, 2015, **5**, 8027.

32 N. Kyung-Wan, B. Seong-Min, H. Enyuan, Y. Xiqian, Z. Youngning, W. Xiaojian, W. Lijun, Z. Yimei, C. Kyung-Yoon and Y. Xiao-Qing, *Adv. Funct. Mater.*, **23**, 1047–1063.

33 Z. Gong and Y. Yang, *J. Energy Chem.*, 2018, **27**, 1566–1583.

34 R. E. Ruther, H. Zhou, C. Dhital, K. Saravanan, A. K. Kercher, G. Chen,

A. Huq, F. M. Delnick and J. Nanda, *Chem. Mater.*, 2015, **27**, 6746–6754.

35 S. Kuppan, Y. Xu, Y. Liu and G. Chen, *Nat. Commun.*, 2017, **8**, 14309.

36 W.-S. Yoon, M. Balasubramanian, K. Y. Chung, X.-Q. Yang, J. McBreen, C. P. Grey and D. A. Fischer, *J. Am. Chem. Soc.*, 2005, **127**, 17479–17487.

37 C. Rumble, T. E. Conry, M. Doeff, E. J. Cairns, J. E. Penner-Hahn and A. Deb, *J. Electrochem. Soc.*, 2010, **157**, A1317–A1322.

38 W. E. Gent, Y. Li, S. Ahn, J. Lim, Y. Liu, A. M. Wise, C. B. Gopal, D. N. Mueller, R. Davis, J. N. Weker, J.-H. Park, S.-K. Doo and W. C. Chueh, *Adv. Mater.*, 2016, **28**, 6631–6638.

39 M. Lécuyer, J. Gaubicher, A. L. Barrès, F. Dolhem, M. Deschamps, D. Guyomard and P. Poizot, *Electrochem. commun.*, 2015, **55**, 22–25.

40 C. Sun, J. Liu, Y. Gong, D. P. Wilkinson and J. Zhang, *Nano Energy*, 2017, **33**, 363–386.

41 Q. Hu, *Nature*, 2015, **526**, Sponsor Feature.

42 K. Jarvis, C. C. Wang, M. Varela, R. R. Unocic, A. Manthiram and P. J. Ferreira, *Chem. Mater.*, 2017, **29**, 7668–7674.

43 S.-K. Jung, H. Gwon, J. Hong, K.-Y. Park, D.-H. Seo, H. Kim, J. Hyun, W. Yang and K. Kang, *Adv. Energy Mater.*, 2014, **4**, 1300787.

44 H. Zhang, K. Karki, Y. Huang, M. S. Whittingham, E. A. Stach and G. Zhou, *J. Phys. Chem. C*, 2017, **121**, 1421–1430.

45 L. Mu, R. Lin, R. Xu, L. Han, S. Xia, D. Sokaras, J. D. Steiner, T. C. Weng, D. Nordlund, M. M. Doeff, Y. Liu, K. Zhao, H. L. Xin and F. Lin, *Nano Lett.*, 2018, **18**, 3241–3249.

46 J. W. Boyd, P. W. Schmalzl and L. L. Miller, *J. Am. Chem. Soc.*, 1980, **102**, 3856–3862.

47 C. Shen, D. Xiong, L. D. Ellis, K. L. Gering, L. Huang and J. R. Dahn, *J. Electrochem. Soc.*, 2017, **164**, A3349–A3356.

48 L. D. Ellis, I. G. Hill, K. L. Gering and J. R. Dahn, *J. Electrochem. Soc.*, 2017, **164**, A2426–A2433.

49 S. S. Zhang, K. Xu and T. R. Jow, *J. Power Sources*, 2006, **159**, 702–707.

50 L. D. Ellis, J. Xia, A. J. Louli and J. R. Dahn, *J. Electrochem. Soc.*, 2016, **163**, A1686–A1692.

51 T. Doi, Y. Shimizu, M. Hashinokuchi and M. Inaba, *J. Electrochem. Soc.*, 2016, **163**, A2211–A2215.

52 X. Zuo, C. Fan, X. Xiao, J. Wu, J. Nan and J. Liu, *J. Electrochem. Soc.*, 2013, **160**, A1199–A1204.

53 T. Doi, Y. Shimizu, M. Hashinokuchi and M. Inaba, *J. Electrochem. Soc.*, 2017, **164**, A6412–A6416.

54 Z. Lu, L. Yang and Y. Guo, *J. Power Sources*, 2006, **156**, 555–559.

55 J. L. Tebbe, A. M. Holder and C. B. Musgrave, *ACS Appl. Mater. Interfaces*, 2015, **7**, 24265–24278.

56 D. Aurbach, B. Markovsky, G. Salitra, E. Markevich, Y. Talyossef, M. Koltypin, L. Nazar, B. Ellis and D. Kovacheva, *J. Power Sources*, 2007, **165**, 491–499.

57 L. C. K. G. G. Amatucci, J. M. Tarascon, *Electrochem. Soc.*, 1996, **143**, 1114–1123.

58 M. Aykol, S. Kim, V. I. Hegde, D. Snydacker, Z. Lu, S. Hao, S. Kirklin,

D. Morgan and C. Wolverton, *Nat. Commun.*, 2016, **7**, 1–12.

59 D. Zhang, L. Zhang, K. Yang, H. Wang, C. Yu, D. Xu, B. Xu and L.-M. Wang, *ACS Appl. Mater. Interfaces*, 2017, **9**, 36886–36896.

60 H. J. Noh, S. Youn, C. S. Yoon and Y. K. Sun, *J. Power Sources*, 2013, **233**, 121–130.

61 S. M. Webb, *Phys. Scr.*, 2005, 1011.

62 A. Panday, S. Mullin, E. D. Gomez, N. Wanakule, V. L. Chen, A. Hexemer, J. Pople and N. P. Balsara, *Macromolecules*, 2009, **42**, 4632–4637.

63 A. E. Javier, S. N. Patel, D. T. Hallinan, V. Srinivasan and N. P. Balsara, *Angew. Chemie - Int. Ed.*, 2011, **50**, 9848–9851.

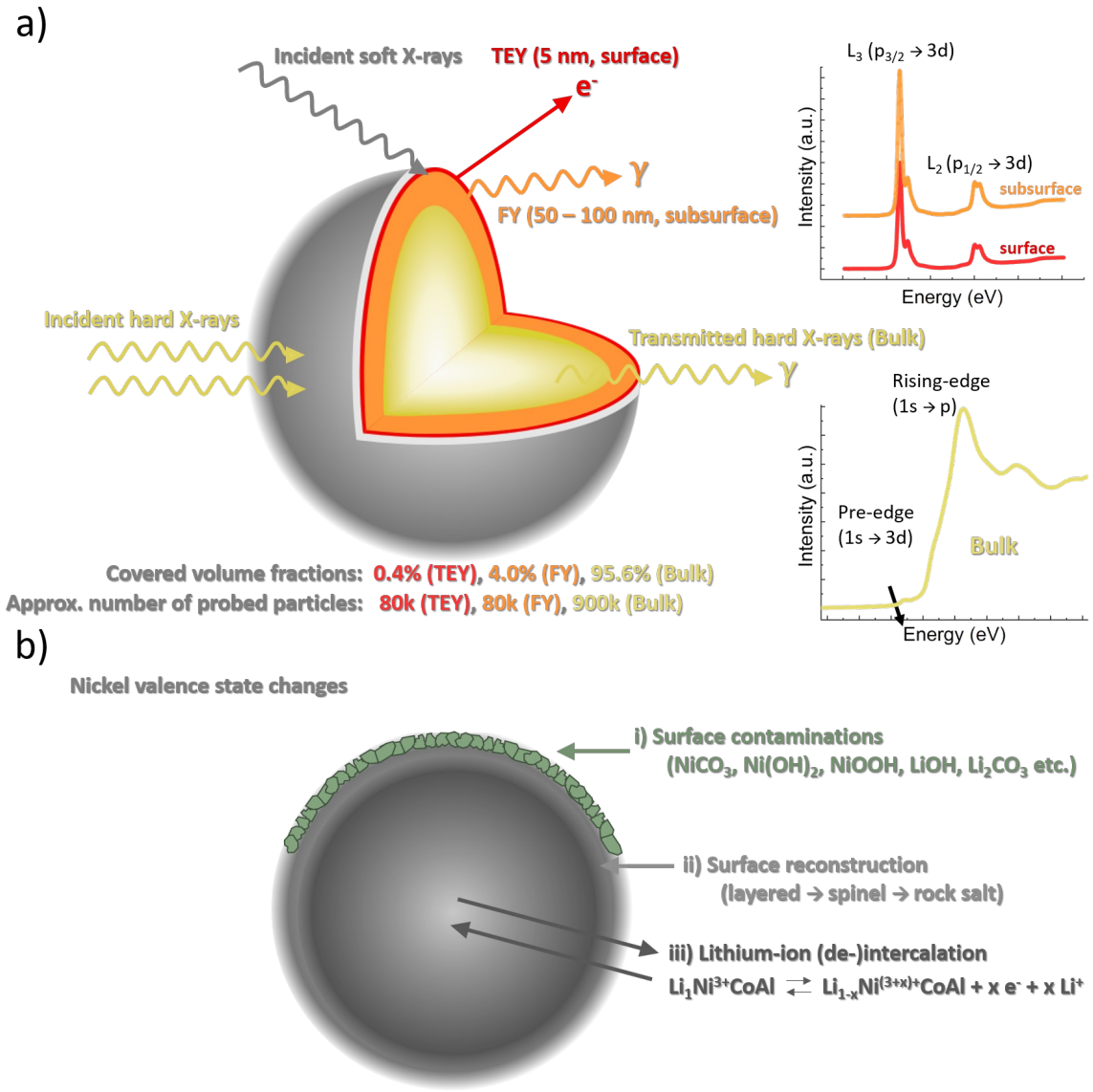

Figure 1. (a) Conceptual overview of synchrotron-based soft and hard X-ray absorption spectroscopy. While soft X-rays (approx. 250 eV – 1200 eV) have a very low penetration depth and are very surface sensitive (up to 100 nm), hard X-rays (> 5 keV) are bulk sensitive and travel through the entire material. Information on the oxidation state can be retrieved either from the surface (soft XAS) or the bulk (hard XAS). (b) Possible nickel valence state changes due to: (i) Formation of surface contaminations upon air exposure; (ii) Surface reconstruction leading to phase

transformation from layered to rock-salt (with simultaneous loss of oxygen); (iii) (De-)intercalation of lithium-ions (from) into the oxide.

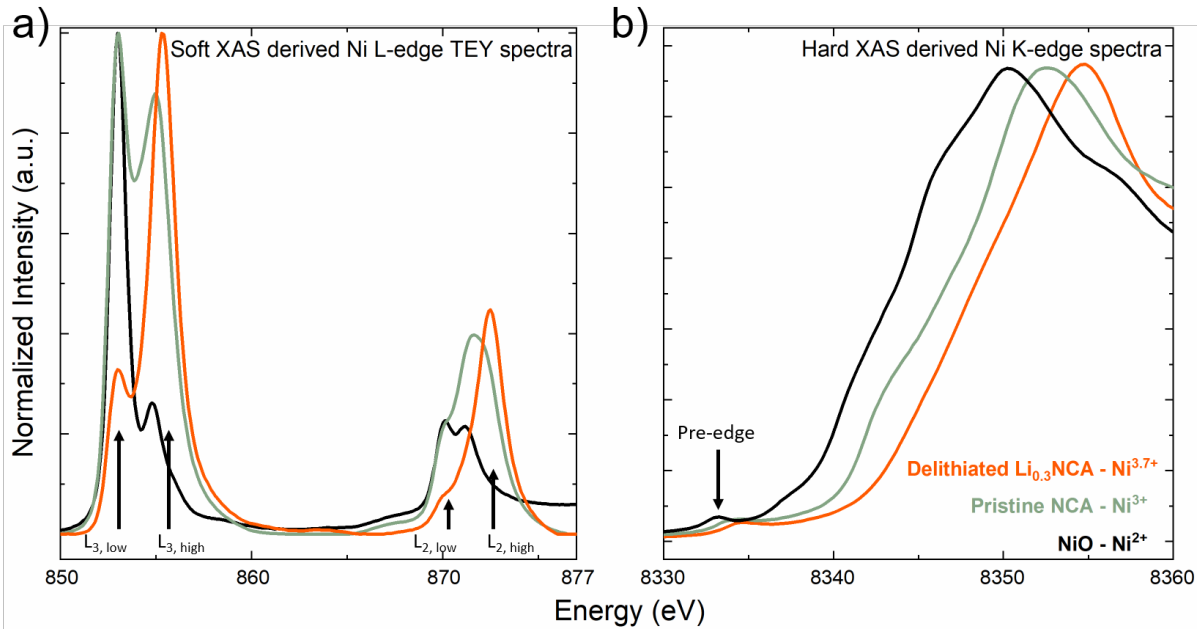

Figure 2. (a) Soft XAS derived TEY mode spectra for NiO (2+), pristine NCA (3+), and delithiated $Li_{0.3}$NCA (3.7+) showing the differences in the L_3 and L_2 peaks as a function of nickel oxidation state in the surface of the material. (b) Hard XAS absorption K-edge of the same substances show the bulk oxidation state dependency of the Ni K-edge.

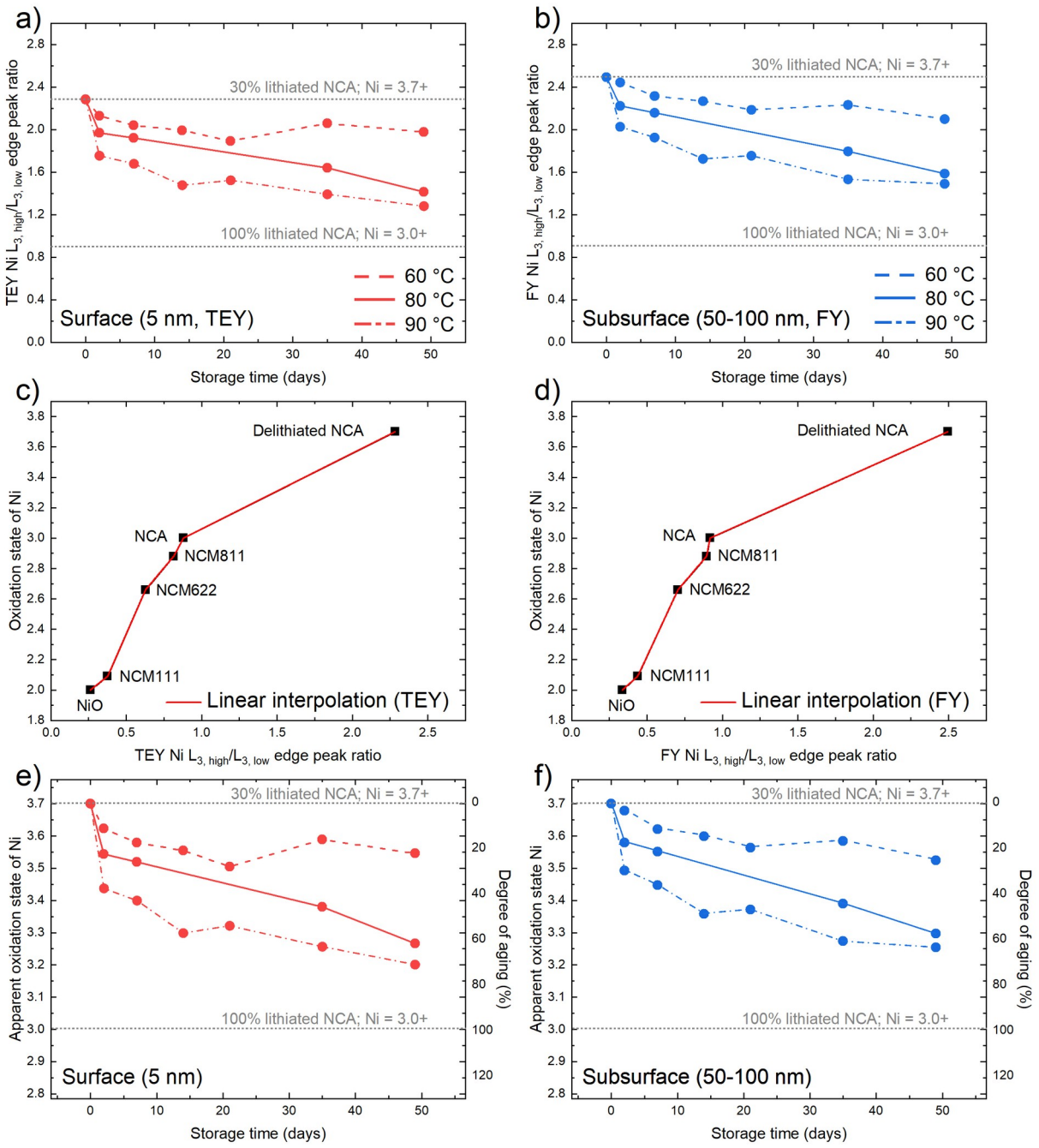

Figure 3. (a) Ni TEY and (b) Ni FY $L_{3,\ high}/L_{3,\ low}$ peak ratios for $Li_{0.3}NCA$ stored at 60, 80 and 90 °C (soft XAS data quality for samples stored for 14 days and 21 days at 80 °C was not sufficient to calculate L_3 ratios). The decomposition relative to the initial peak ratios / oxidation states of delithiated NCA and pristine NCA is indicated by the upper and lower dashed lines, respectively. (c) and (d) Linear interpolation for TEY and FY mode, respectively, correlating measured ratios to oxidation states of

nickelate standards. (e) and (f) Apparent oxidation state and degree of aging for aged samples derived via interpolation.

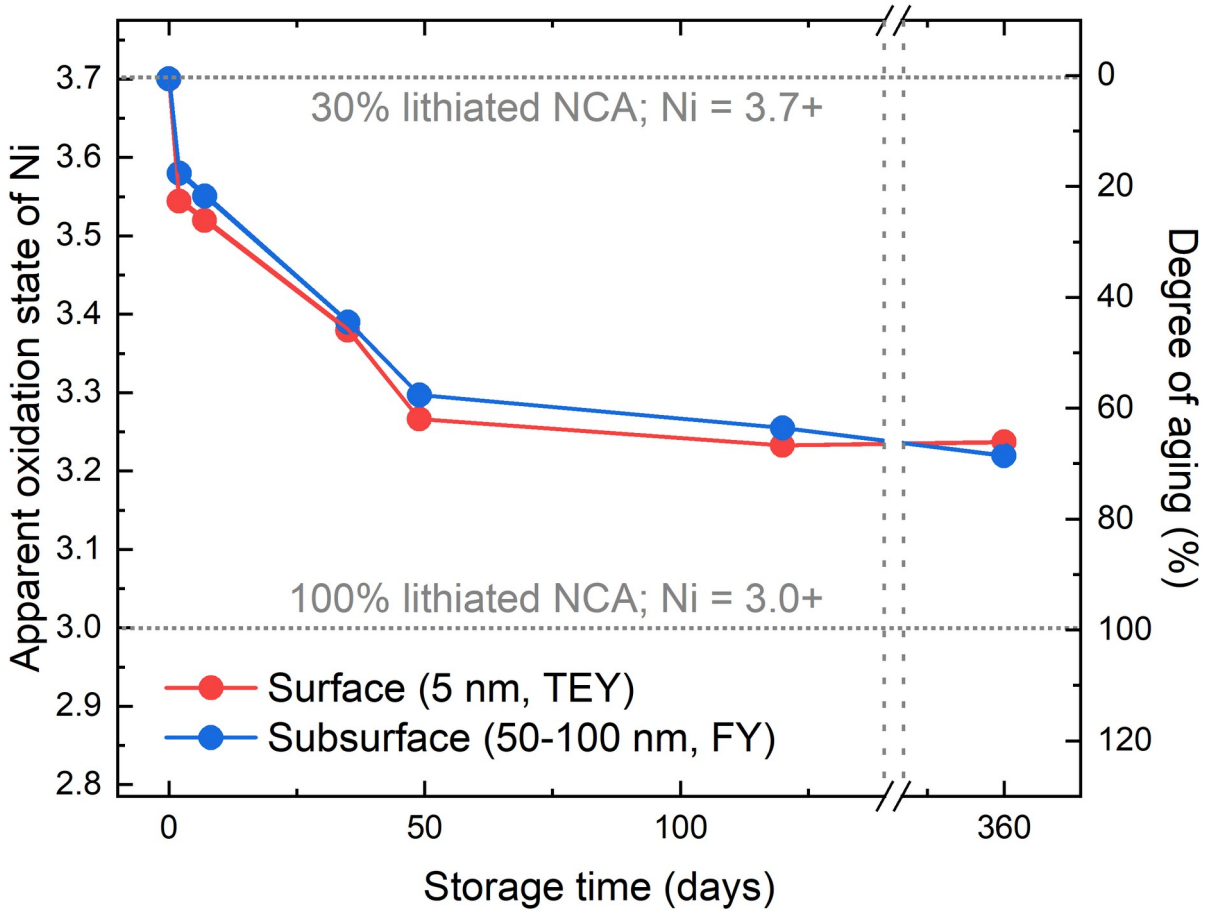

Figure 4. TEY (red) and FY (blue) Ni L_3-edge ratio derived apparent nickel oxidation states and the correlated degrees of aging for $Li_{0.3}NCA$ stored at 80 °C for up to 1 year. Nickel reduction after the initial 49 days is very minimal and comparable with the apparent nickel oxidation state observed after 4 months and 1 year.

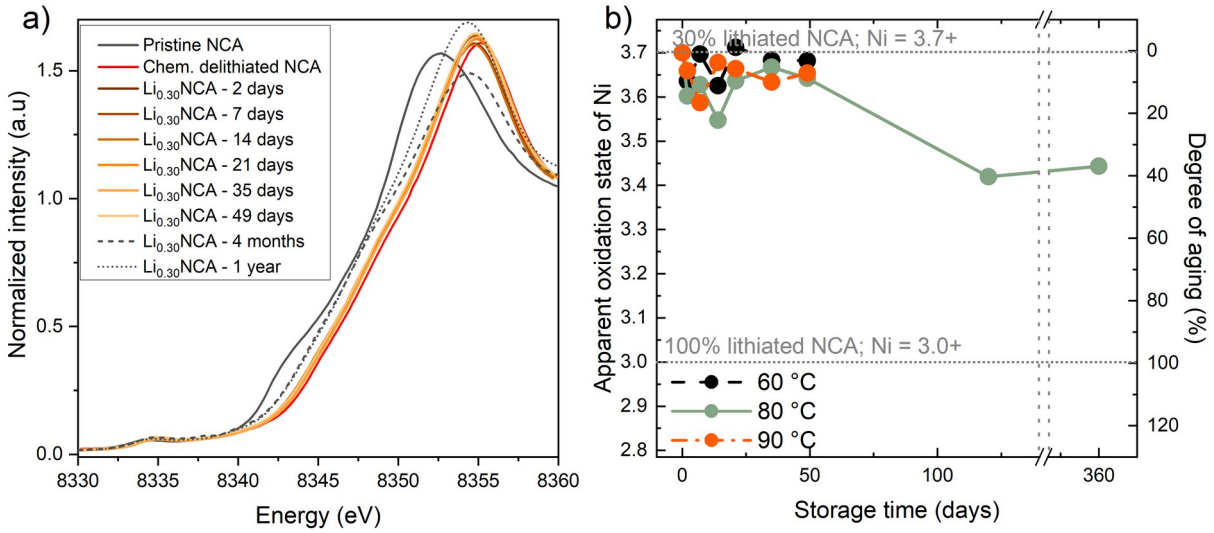

Figure 5. (a) Nickel K-edge XANES spectra for pristine NCA, fresh $Li_{0.3}$NCA, and $Li_{0.3}$NCA stored at 80 °C for various times. (b) Apparent nickel oxidation state and degree of aging as a function of various storage times. No significant reduction of the bulk nickel oxidation state is apparent within the first 49 days of storage. Reduction is only apparent for samples stored for several months, indicating that the core of NCA particles is fairly stable at 80 °C.

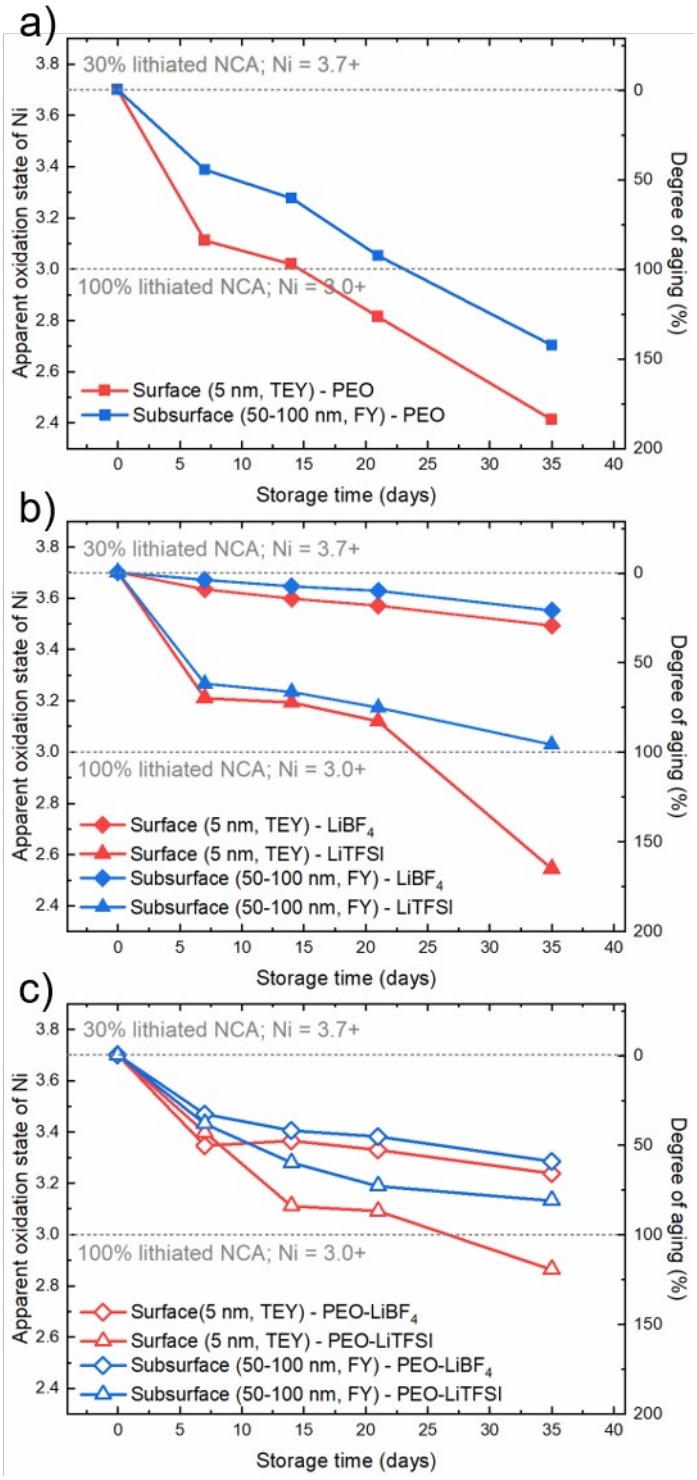

Figure 6. TEY (red) and FY (blue) Ni L_3-edge ratio derived apparent nickel oxidation states and the correlated degrees of aging for $Li_{0.3}NCA$ in combination with (a) PEO, (b) lithium salts, and (c) PEO and lithium salts stored at 80 °C.

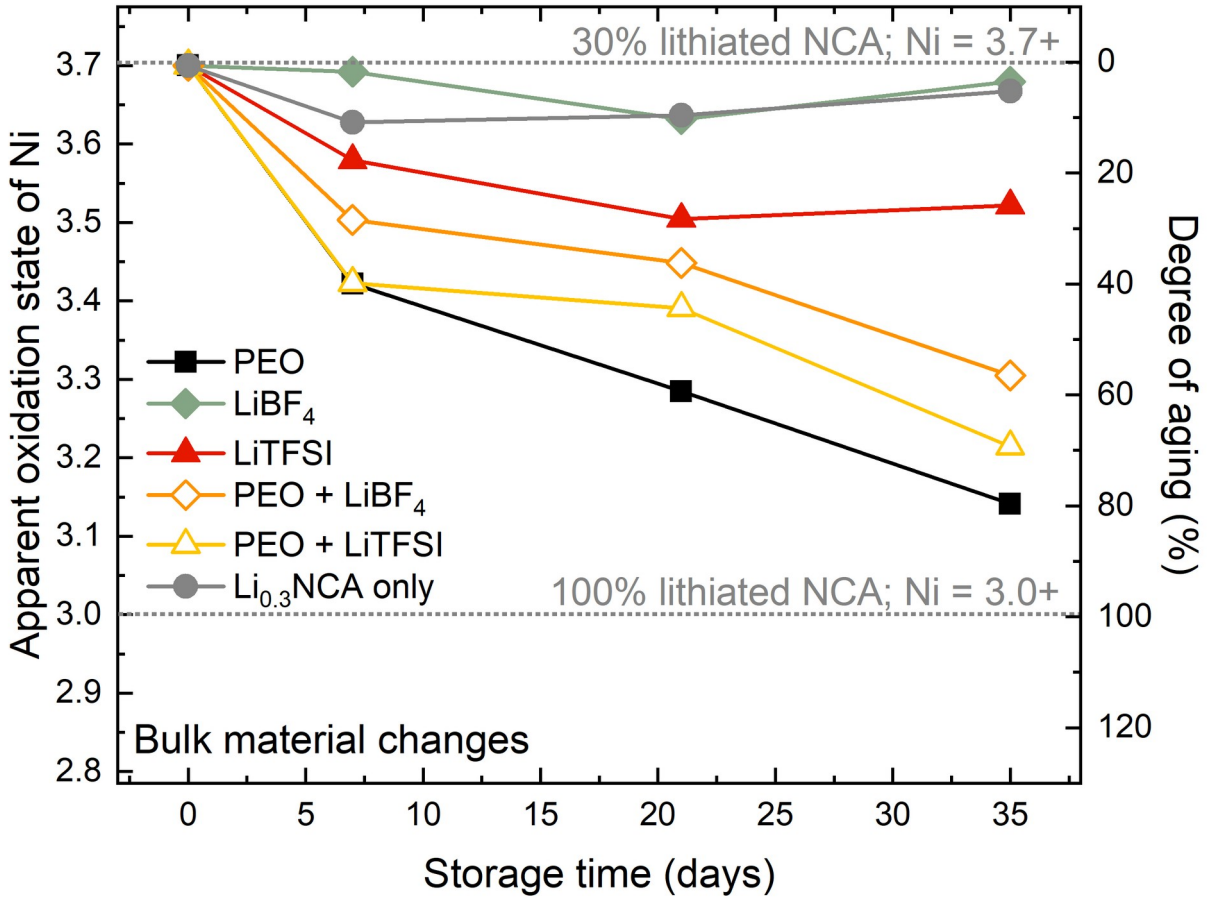

Figure 7. Apparent nickel oxidation state and degree of aging (calculated using nickel XANES spectra) for the bulk material after 35 days of aging at 80 °C.

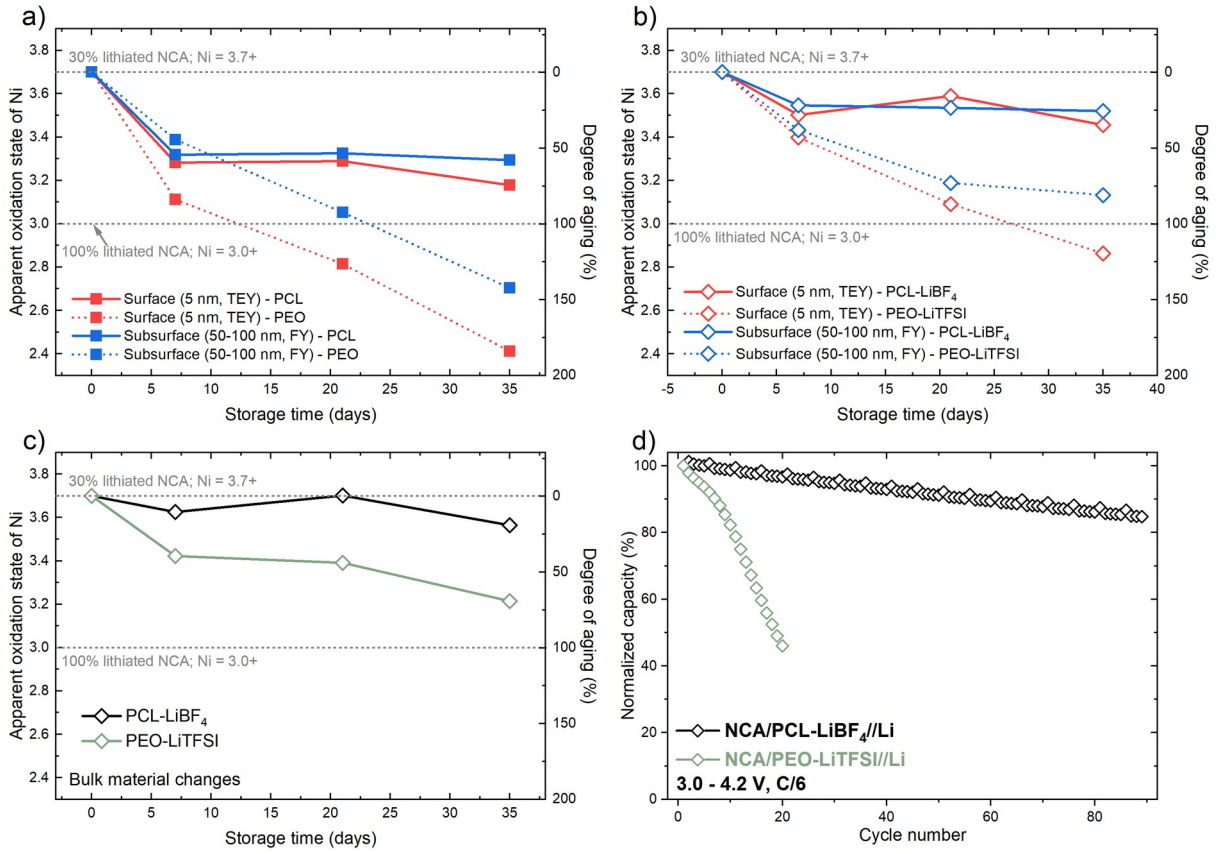

Figure 8. Analysis of surface and bulk degradation for $Li_{0.3}$NCA in combination with PCL and PCL-$LiBF_4$ aged for 35 days at 80 °C. (a) TEY (red) and FY (blue) Ni L_3-edge ratio derived apparent nickel oxidation states and the correlated degrees of aging for $Li_{0.3}$NCA in combination with PCL and PEO. (b) Apparent nickel oxidation state and degree of aging for $Li_{0.3}$NCA blended with PCL-$LiBF_4$ and PEO-LiTFSI. (c) Apparent nickel oxidation state and degree of aging (calculated using nickel XANES spectra) for the bulk of $Li_{0.3}$NCA blended with PCL-$LiBF_4$ and PEO-LiTFSI. (d) Normalized capacities for polymer NCA cells embedded in a PCL-$LiBF_4$ (black) and PEO-LiTFSI (green) polymer matrix.

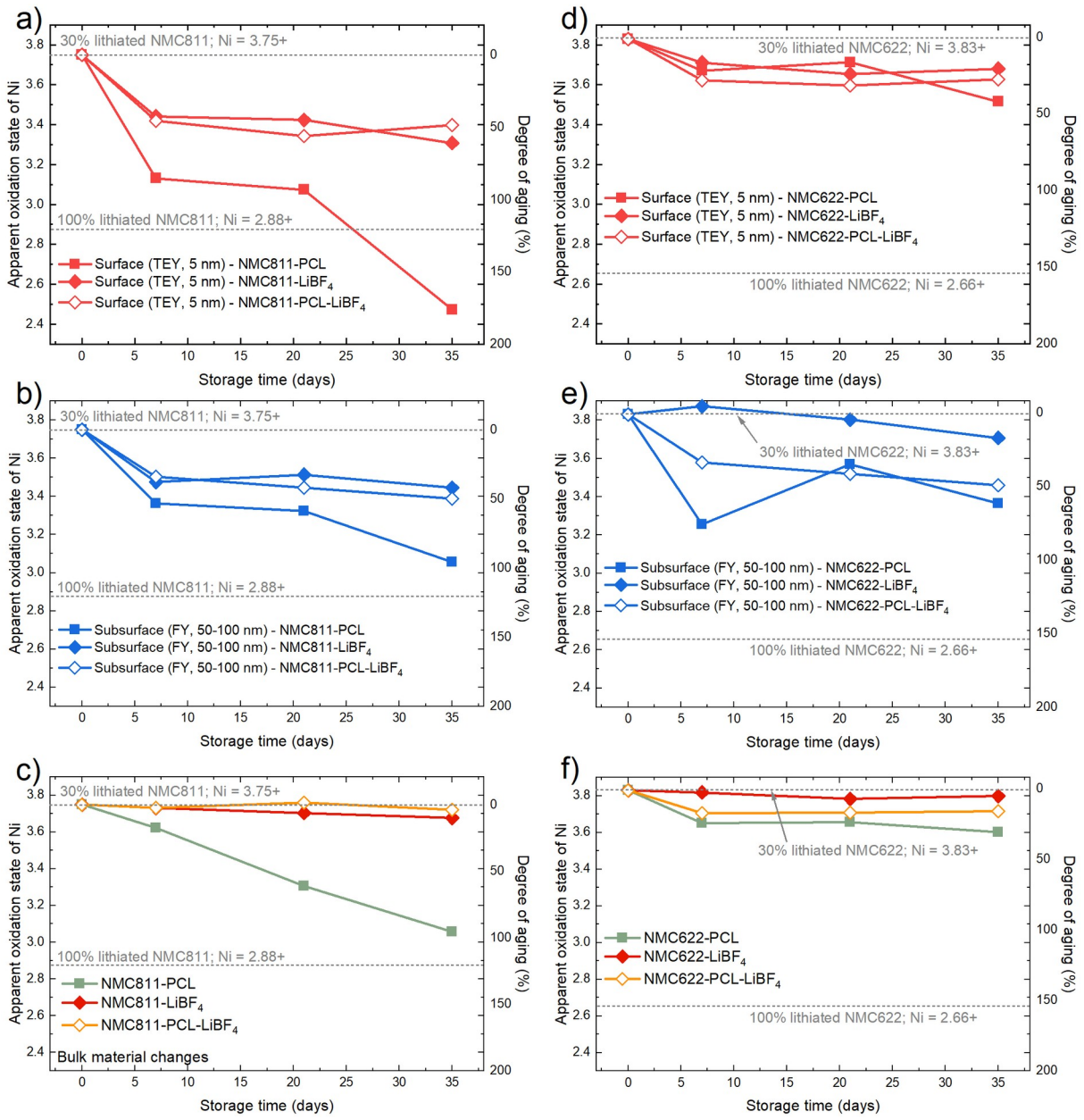

Figure 9. (a) and (b) TEY and FY mode derived apparent oxidation states and correlated degrees of aging for delithiated NMC811 in combination with PCL, $LiBF_4$, and both stored at 80 °C for 7 days, 21 days and 35 days, respectively. (c) Hard XAS derived apparent nickel oxidation states and correlated degrees of aging for NMC811 after the named storage times at 80 °C. (d) and (e) TEY and FY mode derived apparent oxidation states and correlated degrees of aging for delithiated NMC622 in combination with PCL, $LiBF_4$, and both stored at 80 °C for 7 days, 21 days and 35 days,

respectively. (f) Hard XAS derived apparent nickel oxidation states and correlated degrees of aging for NMC622 after the named storage times at 80 °C.

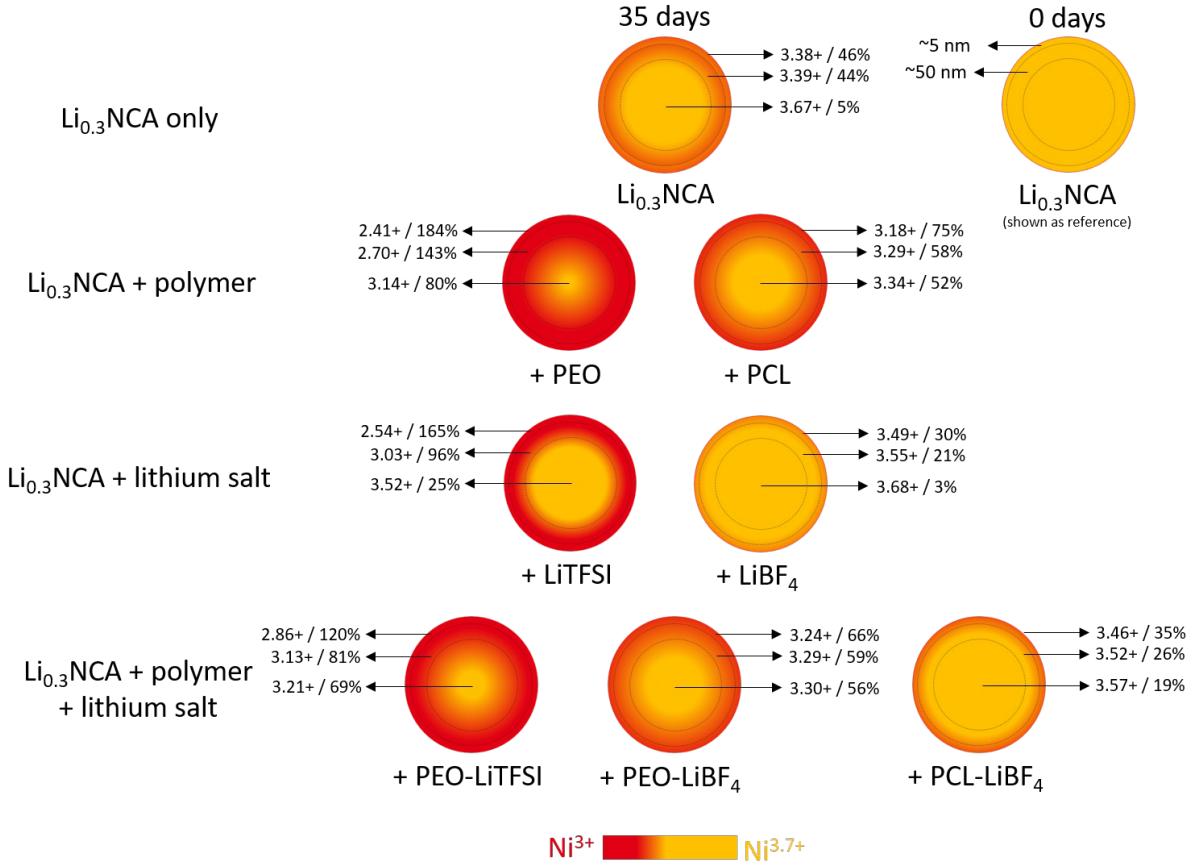

Figure 10. Schematic overview of the initial oxidation state retention in surface and subsurface, and bulk after 35 days of storing $Li_{0.3}NCA$ at 80 °C in combination with PEO, PCL and/or lithium salts.